

Detecting squeezing from the fluctuation spectrum of a driven nanomechanical mode

J. S. Huber,¹ G. Rastelli,¹ M. J. Seitner,¹ J. Kölbl,^{1,*} W. Belzig,¹ M. I. Dykman,² and E. M. Weig¹

¹*Department of Physics, University of Konstanz, 78457 Konstanz, Germany*

²*Michigan State University, East Lansing, MI 48824, USA*

(Dated: June 2, 2022)

Squeezing of quantum and classical fluctuations of one of the quadratures of a vibrational mode enables using this quadrature for high precision measurements. Conventionally squeezing is detected by mixing the mode vibrations with a known signal in homodyne detection. In this paper we demonstrate a different approach to revealing and characterizing squeezing. Using a resonantly driven nonlinear nanomechanical resonator with a high quality factor, we show that classical fluctuations about the stable states of forced vibrations are squeezed and that the squeezing can be measured directly by studying the power spectrum of these fluctuations. The measurement does not require any additional signal. Our experimental and theoretical results are in excellent agreement. They directly extend to the quantum domain and demonstrate an unconventional aspect of squeezing.

I. INTRODUCTION

The Heisenberg uncertainty principle sets a fundamental limit on the fluctuations of two conjugate observables, such as position and momentum or the two quadratures of a harmonic oscillator. In the ground state of a harmonic oscillator the uncertainties of the quadratures are equal and minimal, which determines the fundamental quantum limit of their fluctuations. The equality of the uncertainties is a consequence of the time translation symmetry: indeed, changing the time by half the oscillation period leads to the interchange of the quadratures. Squeezing provides a means for redistributing the fluctuations between the quadratures, reducing the uncertainty in one of them below the quantum limit [1, 2]. Quantum squeezing was first detected in quantum optics [3] and recently also in mechanical systems [4–6]. It enables precision measurements surpassing the quantum limit [7–9].

However, the concept of squeezing of fluctuations in vibrational systems is not limited to the quantum regime. Classical noise squeezing promises to reduce heating in computers [10] and represents an important asset for precision sensing [11–13] enabling the advent of a new generation of nanomechanical detectors at room temperature. It is frequently accomplished using parametric pumping or radiation pressure and has been demonstrated for microwave [14, 15] and mechanical [13, 16–21] resonators as well as for ions in a Penning trap [12]. The classical two-mode squeezing of mechanical resonators by non-degenerate parametric amplification has been also reported [22–24].

Beyond parametric amplifiers, one of the most simple systems that should display squeezing is a resonantly driven Duffing resonator [25–28]. The squeezing here is in many respects qualitatively different from what happens in parametric amplifiers, as it entirely relies on the vi-

bration nonlinearity. To date, squeezing of thermal fluctuations of a driven Duffing resonator is yet to be observed. An experiment under additional noise injection found a bound on the resulting non-thermal squeezing for a driven resonator but only when the resonator was close to the cusp bifurcation point at which the two stable vibrational branches merge together [29].

The measurement of a squeezed state naturally implies the measurement of the individual quadratures of the vibrations, which is accomplished by controlling the phase between the vibrations and an injected signal. The commonly employed method to detect squeezing is a homodyne measurement. This technique has been used in all previous demonstrations of quantum or classical noise squeezing we are aware of, be it the case of a parametric amplifier or a Duffing resonator [3–6, 12–24, 29].

Our experiment demonstrates a way to reveal and characterize a squeezed state in a single shot measurement. The experiment is done in the classical regime, where the fluctuations are thermal. As we show, thermal squeezing is directly manifested in the power spectrum of a driven Duffing resonator. The squeezing parameter can be extracted from a single spectrum recorded in the vicinity of the driving frequency. This obviates the need to accumulate datasets to reconstruct the elliptic phase space distribution of the noise in the two quadratures, as it is the case in a homodyne measurement. In addition, we find that the squeezing of thermal fluctuations of a resonantly driven nonlinear resonator is a generic effect, it is not limited to a narrow vicinity of the cusp point studied previously [29].

Physically, the fluctuation squeezing is a consequence of the breaking of the time translation symmetry by the periodic drive. In our system, fluctuating are the amplitude and phase of the forced vibrations of the resonator. The average values of the amplitude and phase in a stable state are determined by the amplitude and phase of the driving field. Therefore both are fixed, thus providing a reference point to count the phase off, making the quadratures nonequivalent and their fluctuation intensities different from each other.

* Present address: Department of Physics, University of Basel, 4056 Basel, Switzerland

In our experiment we study the power spectrum of a high quality factor nanomechanical resonator at room temperature. Under sufficiently strong driving the power spectrum shows two perfectly resolved peaks symmetrically located on the opposite sides of the driving frequency. The ratio of the areas of these satellite peaks is expected to directly give the squeezing parameter [27, 28, 30]. The onset of satellite peaks was reported in a previous experiment [31], however the satellite peaks were not resolved and, hence, it was impossible to extract their areas, in spite of the injection of an external noise.

Our experimental results agree, with no adjustable parameters, with a theoretical model which extends the one discussed in [25–27, 32]. En passant, we remark that, in our experiment, the injection of an auxiliary noise is not required to reveal the signatures of the squeezed state as in the previous homodyne detection of noise squeezing [29] or power spectra measurements [31].

We also use our driven resonator to explore another effect that occurs in nonequilibrium systems with coexisting stable states. For an equilibrium dynamical system such states can be thought of as the minima of a potential in which the system moves. Fluctuations cause switching between the states, forming a distribution over them. For a small fluctuation intensity, the state populations are exponentially different: in an equilibrium system, this difference is given by the Boltzmann factor that contains the difference between the potential minima divided by $k_B T$. Only in a narrow range where the minima are of almost equal depth are they almost equally populated, an analog of the first order phase transition.

Generically, a nonequilibrium system does not have detailed balance and cannot be mapped onto a Brownian particle in a potential well. Still, it can display an analog of a kinetic phase transition where the state populations are almost equal [25, 33]. A resonantly driven bistable classical oscillator is a system for which it was predicted where such a transition occurs [25]. Our nanoresonator allows us to find the kinetic phase transition in a system lacking detailed balance and thus to quantitatively test a major aspect of the theory of fluctuations in such systems.

II. EXPERIMENTAL SYSTEM

The classical nanomechanical Duffing resonator is realized by a freely-suspended silicon nitride string fabricated on a fused silica substrate [35] whose material parameters are reported in literature [36, 37]. The string under investigation is 270 nm wide, 100 nm thick and 55 μm long, like the one depicted in Fig. 1a. Owing to their strong intrinsic tensile pre-stress, these nanostring resonators exhibit ultra-high quality factors of several 100,000 at room temperature [35, 38]. Dielectric transduction combined with a microwave cavity-enhanced heterodyne detection scheme is implemented via two adjacent gold electrodes also apparent in Fig. 1a. The microwave cavity is

pumped on resonance at ≈ 3.6 GHz to enable displacement detection while avoiding unwanted dynamical back-action effects. The application of a dc voltage as well as a near-resonant rf drive tone V_{in} enables actuation and eigenfrequency tuning of the string [35, 39, 40]. Moreover, the applied dc voltage also affects the damping rate and the nonlinearity, and introduces strong coupling between the out-of-plane and the in-plane mode when tuned into resonance. For all measurements discussed in the following, a constant dc voltage of 5 V is applied. Under that condition, the fundamental flexural out-of-plane mode can be considered independently, such that the following analysis is done in the single mechanical mode regime. The experiment is performed under vacuum at a pressure of $\leq 10^{-4}$ mbar and at room temperature of 293 K.

III. LINEAR REGIME AND CHARACTERIZATION

The sample is characterized by measuring response curves at various drive powers to calibrate the measurement, see also section II of the Supplementary Material (Sup. Mat.) [34]. A weak drive power allows for the characterization of the system in the linear regime. The frequency response of the resonator is measured as a function of the frequency f_F of the applied rf drive. The measured rf voltage signal is proportional to the resonator's amplitude. The resonance of the fundamental out-of-plane mechanical mode is found at $f_0 = 6.529$ MHz with a linewidth of $2\Gamma/2\pi = 20$ Hz, yielding a quality factor of $Q \approx 325,000$. Note that this high quality factor is crucial for the presented work as it enables driving the resonator to amplitudes large enough to enter the nonlinear regime and to resolve the satellite peaks appearing in the power spectrum, as discussed in the following.

IV. NONLINEAR REGIME AND DUFFING MODEL

Increasing the drive power leads to the well-known Duffing response [41–45]. In this model the vibration of the single mode is described by the displacement $q(t)$ which obeys the equation

$$\ddot{q} + 2\Gamma\dot{q} + \omega_0^2 q + \gamma q^3 = F \cos(\omega_F t) + \xi(t). \quad (1)$$

Here, $\omega_0 = 2\pi f_0$ is the angular eigenfrequency, Γ the damping rate, γ the nonlinearity parameter, F and $\omega_F = 2\pi f_F$ are the amplitude and frequency of the external driving, and $\xi(t)$ is the thermal noise. The effective mass of the resonator is, for the time being, set to $m = 1$. In a stationary vibrational state the coordinate $q(t) = A \cos(\omega_F t + \theta)$ oscillates at the drive frequency with a phase θ with respect to the drive. The vibration amplitude A is given by the solution of the cubic equation $A_j^2 \{[\delta\omega - 3\gamma A_j^2/(8\omega_0)]^2 + \Gamma^2\} = F^2/4\omega_0^2$, where

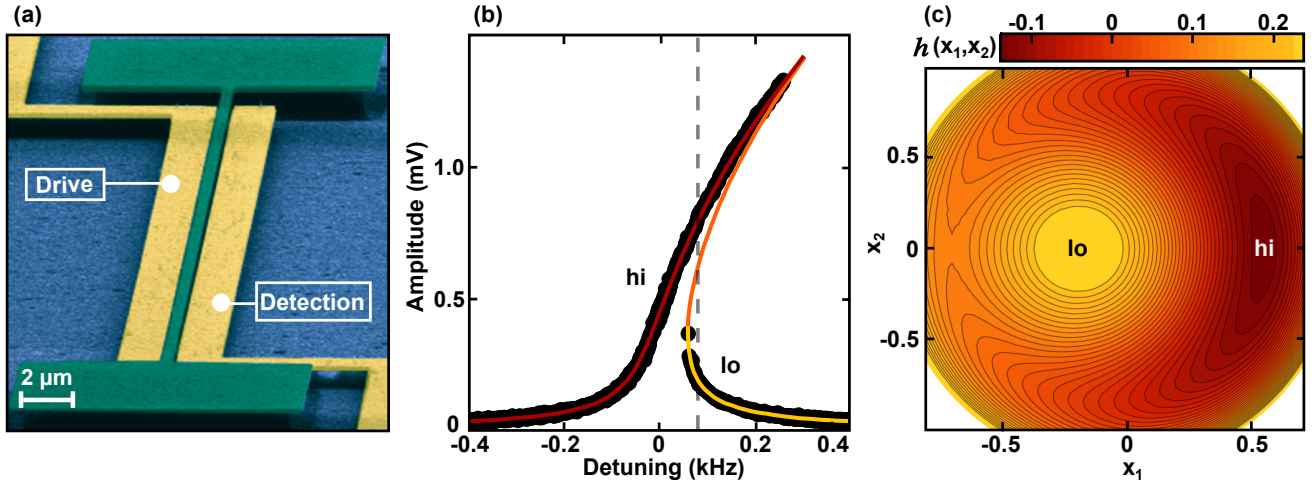


Figure 1. (a) Scanning electron micrograph of the doubly clamped silicon nitride string resonator (green) and two adjacent gold electrodes (yellow) for dielectric control. Schematic of electronic setup is detailed in the Sup. Mat. [34]. (b) Duffing response curve for an external drive of -31 dBm (black dots) and fit of Eq. (1). The red (yellow) line denotes the high (low) amplitude solution marked “hi” (“lo”), while the orange line represents the unstable solution. Dashed gray line indicates the theoretically calculated critical switching point. (c) Phase space representation of the effective Hamiltonian function $h(x_1, x_2)$. Indicated are the high (“hi”, red) and low (“lo”, yellow) amplitude solution. The Hamiltonian function $h(x_1, x_2)$ scaled by $8\omega_F\delta\omega^2/(3\gamma)$ is plotted using the parameter $\sqrt{3\gamma F^2}/(32\omega_F^3\delta\omega^3) = 0.013$, corresponding to the dashed line in (b), whereas the coordinate axes are scaled with $\sqrt{8\omega_F\delta\omega}/(3\gamma)$.

$\delta\omega = \omega_F - \omega_0$ is the frequency detuning, $|\delta\omega| \ll \omega_0$ for the considered near-resonant driving. The Duffing equation reflects the fact that the vibration frequency of a nonlinear resonator depends on its amplitude. It can have one or three positive solutions. In the latter case, only the solutions with the largest and the smallest amplitude, A_{hi} and A_{lo} , are stable. An example of the measured amplitude as a function of the frequency detuning $\delta\omega$ is shown in Fig. 1b by black dots. The solid line represents a fit of the Duffing model (Eq. (1)). Only one fitting parameter, the nonlinear Duffing parameter $\tilde{\gamma}$ rescaled to units of $1/V^2s^2$ is required since the eigenfrequency ω_0 , the damping rate Γ as well as the calibration of the driving force F are known from the characterization in the linear regime [34]. Nonlinear response curves obtained for different values of the rf drive power $P = -31$ dBm (shown in Fig. 1b), -30 dBm (shown in the Sup. Mat.), -25 dBm, -20 dBm and -18 dBm are fit using a single value $\tilde{\gamma} = 2.35(15) \cdot 10^{15} V^{-2}s^{-2}$. Further, the backbone of the Duffing curves allows converting the measured amplitude signal (in volts) into real displacement (nanometers) [46]. This method relies on the nonlinear Duffing parameter arising from the geometric nonlinearity of the string, $\gamma^* = 1.54 \cdot 10^{26} m^{-2}s^{-2}$, which corresponds to $2.28 \cdot 10^{15} V^{-2}s^{-2}$ in good agreement with $\tilde{\gamma}$ extracted from the data [34].

V. THEORY: SQUEEZING IN THE POWER SPECTRUM

The theoretical analysis of the resonator dynamics is done by switching to the rotating frame, $q(t) = x_1(t)\cos(\omega_F t) + x_2(t)\sin(\omega_F t)$ and $\dot{q}(t) = -\omega_F[x_1(t)\sin(\omega_F t) - x_2(t)\cos(\omega_F t)]$ where the quadratures $x_1(t)$ and $x_2(t)$ are new conjugate variables. Using the standard rotating wave approximation (RWA), one finds that the time evolution of these variables is described by the equations

$$\dot{x}_1 = \frac{\partial h(x_1, x_2)}{\partial x_2} - \Gamma x_1, \quad (2)$$

$$\dot{x}_2 = -\frac{\partial h(x_1, x_2)}{\partial x_1} - \Gamma x_2, \quad (3)$$

with the Hamiltonian function

$$h(x_1, x_2) = \frac{3\gamma}{32\omega_F} (x_1^2 + x_2^2)^2 - \frac{\delta\omega}{2} (x_1^2 + x_2^2) - \frac{F}{2\omega_F} x_1. \quad (4)$$

In writing Eqs. (2), (3) we have, for the time being, disregarded the noise. A contour plot of the function $h(x_1, x_2)$ in the range of the bistability is shown in Fig. 1c.

A remarkable feature of our high Q nanostring resonator is that the damping rate Γ is small not only compared to the eigenfrequency ω_0 , but also compared to the frequency detuning $\delta\omega$ and/or the typical frequency change due to the nonlinearity $\gamma A_j^2/\omega_F$. Therefore the damping can be treated as a small perturbation of the Hamiltonian dynamics of an auxiliary “particle” with coordinate x_1 and momentum x_2 . In this limit of weak

damping, the extrema $j = hi, lo$ of h correspond to the two stable states of forced vibrations [47]. At the extrema, $x_{2,j} = 0$, whereas $|x_{1,j}| = A_j$ gives the vibration amplitude, if one disregards corrections $\propto \Gamma^2$. The Hamiltonian dynamics for $\Gamma = 0$ is characterized by the frequency ω_j of small-amplitude vibrations about the extrema of $h(x_1, x_2)$,

$$\omega_j = \sqrt{\omega_j^{(1)} \omega_j^{(2)}}, \quad (5)$$

where $\omega_j^{(1)} = 3\gamma A_j^2/8\omega_F - \delta\omega$ and $\omega_j^{(2)} = 9\gamma A_j^2/8\omega_F - \delta\omega$ (we note that $\omega_j^{(1,2)}$ can be positive or negative, but their product is positive). The frequency is different in the high- and low-amplitude states. In the considered weak-damping case $\Gamma \ll \omega_j$.

We now reintroduce noise into the equations for the quadratures and discuss thermal fluctuations about the stable states. Even though the nanoresonator under investigation is small, thermal fluctuations at room temperature are weak. If there is no driving ($F = 0$ in Eq. (4)), the mean-square values of the quadratures are the same, and for the considered weak nonlinearity $\langle x_1^2 \rangle = \langle x_2^2 \rangle = k_B T / \omega_0^2$.

To analyze the squeezing of fluctuations about the states of forced vibrations for the case of weak damping, we linearize the equations of motion about the stable vibrational states (x_{1j}, x_{2j}) keeping the lowest-order terms in the decay rate Γ (such linearization may be insufficient in the case of extremely weak damping, as discussed in section I.E of the Sup. Mat. [34]). From Eqs. (1), (2) and (3), the resulting equations for the increments $\delta x_{1,2}$ in the presence of noise are,

$$\delta \dot{x}_1 = \omega_j^{(1)} \delta x_2 - \Gamma (1 + \mu_j) \delta x_1 + \xi_{x_1}(t), \quad (6)$$

$$\delta \dot{x}_2 = -\omega_j^{(2)} \delta x_1 - \Gamma (1 - \mu_j) \delta x_2 + \xi_{x_2}(t). \quad (7)$$

Here, $\mu_j = 6\gamma A_j^2 / (3\gamma A_j^2 - 8\omega_F \delta\omega)$ and we have disregarded terms $\propto \Gamma^2$. Functions $\xi_{x_1}(t)$ and $\xi_{x_2}(t)$ describe the noise that drives the quadratures. In the phenomenological model Eq. (1) these functions are given by the real and imaginary parts of $i\xi(t) \exp(i\omega_F t) / \omega_F$. If the noise comes from the same coupling to a thermal bath that leads to the vibration decay, on the time scale $\gg \omega_F^{-1}$ it is zero-mean, Gaussian and δ -correlated, and the components ξ_{x_1}, ξ_{x_2} are independent and have equal intensity, $\langle \xi_{x_1}(t) \xi_{x_1}(0) \rangle = \langle \xi_{x_2}(t) \xi_{x_2}(0) \rangle = (2\Gamma k_B T / \omega_0^2) \delta(t - t')$.

A qualitative feature of the driven resonator is that the mean-square fluctuations of the in-phase and quadrature components of the coordinate are no longer equal and can be smaller than in the absence of the drive. This is a squeezing effect. As shown in the Sup. Mat. [34]

$$\langle \delta x_1^2 \rangle = \frac{k_B T}{2m\omega_F^2} (1 + e^{-4\varphi_j}), \quad (8)$$

$$\langle \delta x_2^2 \rangle = \frac{k_B T}{2m\omega_F^2} (1 + e^{4\varphi_j}), \quad (9)$$

where the expression

$$\exp(4\varphi_j) = \omega_j^{(1)} / \omega_j^{(2)} \quad (10)$$

defines the squeezing parameter φ_j . Here, we have reintroduced the effective mass of the nanoresonator m to facilitate the comparison with the experiment. In the absence of driving, we find $A_j = 0$ and thus $\varphi_j = 0$, such that we recover the equipartition theorem, $\langle \delta x_1^2 \rangle = \langle \delta x_2^2 \rangle$. For the large-amplitude stable state $\varphi_j \equiv \varphi_{hi} > 0$, whereas for the small-amplitude state $\varphi_j \equiv \varphi_{lo} < 0$. Obviously, the maximum squeezing attainable is a 50% reduction of the squeezed quadrature according to Eqs. (8) and (9).

Remarkably the squeezing appears directly in the power spectrum of the resonator [27, 30]. In the weak damping limit $\Gamma \ll \omega_j$, one obtains

$$Q_j(\omega) \approx \frac{\Gamma k_B T}{4\pi m\omega_F^2} \frac{\cosh 2\varphi_j (\cosh 2\varphi_j \pm 1)}{(\omega - \omega_F \mp \Theta_j \omega_j)^2 + \Gamma^2} \quad \text{for } |\omega - \omega_F \mp \Theta_j \omega_j| \ll \omega_j, \quad (11)$$

with $\Theta_{hi} = +1$ for the large-amplitude stable state and $\Theta_{lo} = -1$ for the small-amplitude stable state, respectively [34]. The power spectrum $Q_j(\omega)$ consists of two Lorentzian peaks centered at the frequencies $\omega_F \pm \Theta_j \omega_j$ with the half width given by the damping rate of resonator in the absence of driving Γ . They can be thought of as the Stokes and anti-Stokes components of the Raman scattering of the driving field by the small-amplitude vibrations of the resonator near the corresponding stable state. Importantly, the very state is formed by the drive. The ratio of the intensities of the satellite peaks

$$\mathcal{I}_{hi}^{(+)} / \mathcal{I}_{hi}^{(-)} = 1 / \tanh^2(\varphi_{hi}), \quad (12)$$

$$\mathcal{I}_{lo}^{(+)} / \mathcal{I}_{lo}^{(-)} = \tanh^2(\varphi_{lo}), \quad (13)$$

is determined by the squeezing parameter φ_j . The squeezing parameter can thus be directly extracted from the power spectrum. An advantageous feature of the ratios Eqs. (12), (13) is their independence of the temperature. Therefore even if the nanoresonator is slightly heated by the drive, they should not change. We note that, in the quantum regime, $\hbar\omega_0 \gtrsim k_B T$, the power spectra also have two satellite (sideband) peaks, with the ratio of their intensities determined by the squeezing parameters $\varphi_{hi,lo}$ [27, 28, 30]. Squeezing of quantum fluctuations about a metastable state occurs also in a driven oscillator resonantly coupled to a two-level system [48].

VI. EXPERIMENTAL OBSERVATION OF THE THERMAL SQUEEZING IN THE POWER SPECTRUM

To validate these theoretical findings, we apply a resonant sinusoidal drive tone to the fundamental flexural mode of the nanostring ($f_F = f_0$) and record power spectra for different drive powers using a spectrum analyzer

operated in the FFT-mode. Under resonant driving, the resonator has one stable vibrational state, with the parameters in Eqs. (8), (9), (12), and (13) corresponding to the high-amplitude state A_{hi} . Figure 2a displays power spectra for drive powers in the range between -45 dBm and -5 dBm , with a color coded signal power (dBm). The bright, narrow line centered at zero corresponds to forced vibrations at f_F . The drive tone is flanked by two satellite peaks. Their separation from the drive tone is symmetric and increases with drive power. We identify these satellite peaks with the thermal noise-induced small-amplitude vibrations around the stable state of the driven resonator. Thus the peaks should be centered at the frequencies $\omega_F \pm \omega_{\text{hi}}$.

The experimentally observed satellite peaks are compared with the theoretical prediction of Eq. (5) in Fig. 2a, where the calculated positions of the peaks are shown as open red circles. For better visualization, only a few distinct points are plotted. We find the experimental data to coincide with the theory, and also recover the expected scaling of the splitting of the satellite peaks with the drive power $\omega_{\text{hi}} \propto A_{\text{hi}}^2 \propto F^{2/3} \propto P^{1/3}$.

Another remarkable feature of the satellite peaks is apparent from their intensities. Figure 2b depicts a line cut extracted from Fig. 2a at -20 dBm . Each peak is fitted by a Lorentzian with a linewidth of $2\Gamma/2\pi = 20 \text{ Hz}$, as shown in Fig. 2b. As predicted by the theoretical model, this linewidth coincides with that of the linear resonance of the string [34]. Clearly, the satellite peak at higher frequency is much brighter than that at the lower frequency. This observation is in agreement with the theoretical model, which predicts non-equal intensities of the satellite peaks as a result of the classical squeezing of thermal fluctuations.

More precisely, as outlined in Eqs. (12) and (13), for the high-amplitude state A_{hi} , a higher intensity is expected for the satellite peak at the higher frequency. Following the model, the ratio of the areas enclosed by the peaks is simply related to the squeezing parameter φ_j . The areas extracted from the fit are plotted in Fig. 2c as a function of the drive power, where green corresponds to the brighter, higher frequency peak and blue to the lower frequency peak. The experimental data are compared with the theoretical predictions which are shown in Fig. 2c by the red lines [34]. As suggested by the theoretical model, a pronounced difference in the areas is observed. The ratio of the areas is plotted in Fig. 2d, and again, we find very good agreement between the experimental data (black dots) and the theoretical predictions (red line).

The theoretical calculations of the areas and their ratio shown in Fig. 2 are obtained from a more general analysis of the power spectrum. This analysis is not limited to the condition $\Gamma \ll \omega_j$ and thus takes into account the overlapping of the satellite peaks. It is provided in Secs. I C and I D of the Sup. Mat [34]. The ratio of the areas for the limit of small damping, Eqs. (12) and (13), is also included in Fig. 2d as a gray line. In this limit the ratio is independent of the drive power; it provides the fun-

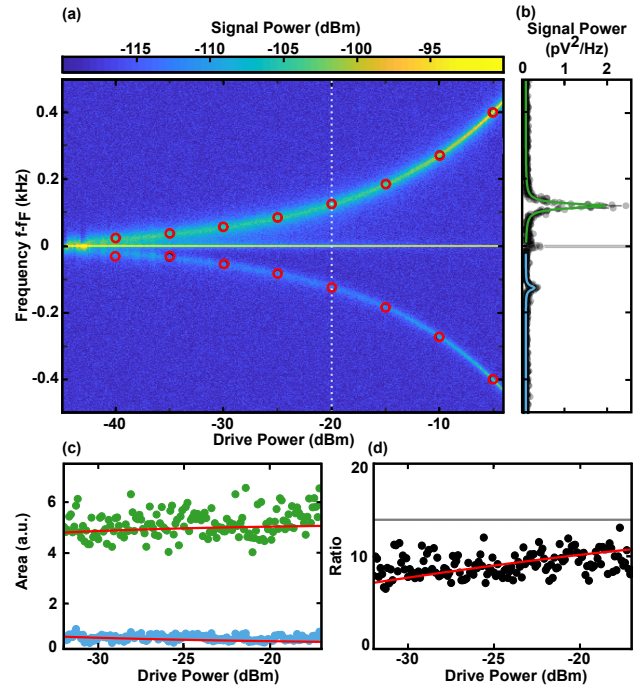


Figure 2. (a) Color coded power spectra showing the increasing splitting of the satellite peaks with the increasing drive power for the drive frequency $f_F = f_0$ where the resonator is monostable. Red open circles denote the calculated positions of the satellite peaks. The central line at $f - f_F = 0$ is plotted with a reduced brightness to improve the visibility of the satellites. (b) Linecut along the bright dotted line in Fig. 2a illustrating the satellite peaks as well as their Lorentzian fits for a drive of -20 dBm . The central line at $f = f_F$ (gray line) is truncated. (c) Area of the high (green) and low (blue) frequency satellite peaks extracted from the Lorentzian fits as a function of the drive power. Red lines show the theoretical prediction that takes into account the partial overlap of the peaks. (d) Ratio of the areas of the satellite peaks as a function of drive power. Red and gray lines show, respectively, the theoretical prediction that takes into account the partial overlap of the peaks (see Sup. Mat [34]) and the one based on Eq. (12).

damental limiting value for the ratio of the areas of the satellite peaks. For our high-Q nanostring resonator, the measured ratio approaches this value as the separation of the peaks increases with the increasing drive power.

According to the theory, the satellite peaks in the power spectrum also depend on the detuning of the drive frequency $f_F - f_0$. We therefore repeat the measurement routine, now for a fixed drive power of -20 dBm and a variable detuning of the drive. The resonator is initialized in the high-amplitude state by sweeping up the drive frequency from 30 kHz below f_0 to the desired f_F before recording the power spectrum.

Figure 3a displays the power spectra as a function of the detuning $f_F - f_0$. For large negative detuning, $f_F - f_0 < 0$, only the satellite peak at a higher frequency can be discerned; its distance from the drive tone f_F increases

with the increasing $-(f_F - f_0)$. For small detuning, both satellite peaks are resolved. They are at equal distances from f_F , which only slightly increase with $f_F - f_0$ for $f_F - f_0 > 0$. In contrast, the intensities of the peaks are increasing. The splitting at zero detuning equals the one shown in the resonantly driven case discussed in Fig. 2a for a drive power of -20 dBm.

Interestingly, the satellite peak at higher frequency vanishes abruptly for the detuning of 190 Hz, whereas the lower frequency one remains. However, the lower frequency peak exhibits a discontinuity at 190 Hz, and continues with a larger splitting, a different slope, and a strongly reduced intensity. At the same detuning of 190 Hz the amplitude at the drive tone drops to a drastically smaller value, as shown in Fig. 3b. This is a signature of the resonator switching from the high-amplitude state A_{hi} to the low-amplitude state A_{lo} . The displayed signal power has been extracted from a linecut in Fig. 3a at the driving frequency, $f = f_F$. Since every power spectrum in Fig. 3a takes more than one minute to be recorded, this represents a much slower measurement than a typical (Duffing) response curve measurement.

The observed satellite peaks on the opposite sides of the critical detuning $\Delta f_{\text{cr}} \equiv (f_F - f_0)_{\text{cr}} \approx 190$ Hz are associated with the high- and low-amplitude state A_{hi} and A_{lo} of the resonator. They are compared in Fig. 3a with the theoretical prediction for the two stable states, which are superposed on the measured data as red and yellow open circles, respectively. In the both states, we find the experiment and the theory to coincide completely.

We repeat the analysis described for the resonantly driven case of Fig. 2 and extract the areas of the high and low frequency satellite peaks for each power spectrum by fitting two Lorentzians (not shown). When the resonator is in the high-amplitude state, i.e. for a detuning below Δf_{cr} , both satellite peaks are resolved and appear for a certain range of detunings. The ratio of the obtained areas of the peaks for this detuning is shown in Fig. 3c as black dots. Like for the resonantly driven case, this quantity is associated with the squeezing parameter.

According to the theory of Sec. V, the ratio of the areas of the peaks depends on the detuning of the drive frequency. For the high-amplitude stable state, it is asymmetric with respect to f_0 and decreases as the detuning varies from negative to positive. The experimental data in Fig. 3c is compared with the theoretical prediction for the weak-damping limit, Eq. (12) (gray line), and for the more general approximation that takes into account the small overlapping of the satellite peaks [34] (red line). Once more, the agreement between the experiment and the theory is remarkable.

Above the switching point, $f_F - f_0 > \Delta f_{\text{cr}}$ the resonator is in the low-amplitude state, and only one satellite peak is resolved. Thus the ratio of the areas of the peaks and thus the squeezing parameter cannot be evaluated here. Notice, however, that the data clearly shows the anticipated reversal of the intensities of the satellite peaks between the two stable solutions, as predicted

by Eq. (12) and (13): While the high frequency satellite peak has a higher intensity for the high-amplitude stable state, the low frequency peak is the dominating one for the low-amplitude state. In addition, while the ratio of the areas of the peaks for the high-amplitude state has decreased to a value ≈ 1 in the vicinity of the switching point f_{cr} , for the low-amplitude state the ratio is large, according to the theory, which explains why the low frequency satellite peak is resolved whereas the high frequency peak cannot be detected.

For a positive or negative detuning exceeding 400 Hz, Fig. 3a exhibits only one peak, and the slope of its frequency vs the drive frequency is -1 . Such slope and a single peak in the power spectrum are expected for an oscillator in the absence of a driving force. Experimentally, for still larger detuning, we are not able to resolve thermal motion of the driven resonator, as is also the case for the undriven resonator. We attribute this to an insufficient displacement sensitivity of the detection setup far away from the driving frequency or in the absence of the drive, while the thermally-induced spectral features are resolved near f_F . Apparently, the displacement sensitivity increases in the presence of the driving, which is likely a consequence of our heterodyne microwave-cavity assisted displacement detection scheme [35].

VII. CRITICAL SWITCHING POINT

Finally, we discuss the switching between the two stable states of the Duffing resonator. It is characterized by two rates, that from the high-amplitude to the low-amplitude state, $W_{\text{hi} \rightarrow \text{lo}}$, and that from the low-amplitude to the high-amplitude state, $W_{\text{lo} \rightarrow \text{hi}}$. At the critical frequency detuning these rates are equal, $W_{\text{hi} \rightarrow \text{lo}} = W_{\text{lo} \rightarrow \text{hi}}$. Respectively, the stationary populations of the stable states are also equal. The rates change with the parameters exponentially strongly. Therefore, away from the critical value of the detuning, the populations of the states are strongly different and only one state is “visible”. If the detuning is slowly varied across the critical value, the oscillator should switch from one state to the other in a very narrow range. For weak damping, $\Gamma \ll \delta\omega$, the theoretical value of the critical detuning [25], in terms of the parameters of the studied nanoresonator, is $\Delta f_{\text{cr}} \approx 904.6 \text{ s}^{-1} (V_{\text{in}}[\text{V}])^{2/3}$. It is shown in Fig. 1b as a vertical dashed gray line at $V_{\text{in}} = 17.8$ mV (-31 dBm).

Experimentally, the interchange of the most probable states at the critical point can only be observed in a slow measurement. Clearly, the response curve shown in Fig. 1b does not reveal this point, since the detuning was swept in the both directions fast enough to allow the system to stay in the metastable high- or low-amplitude state well beyond the critical point, until close to the bifurcation point.

In contrast, the response curve shown in Fig. 3b results from a much slower measurement as described above.

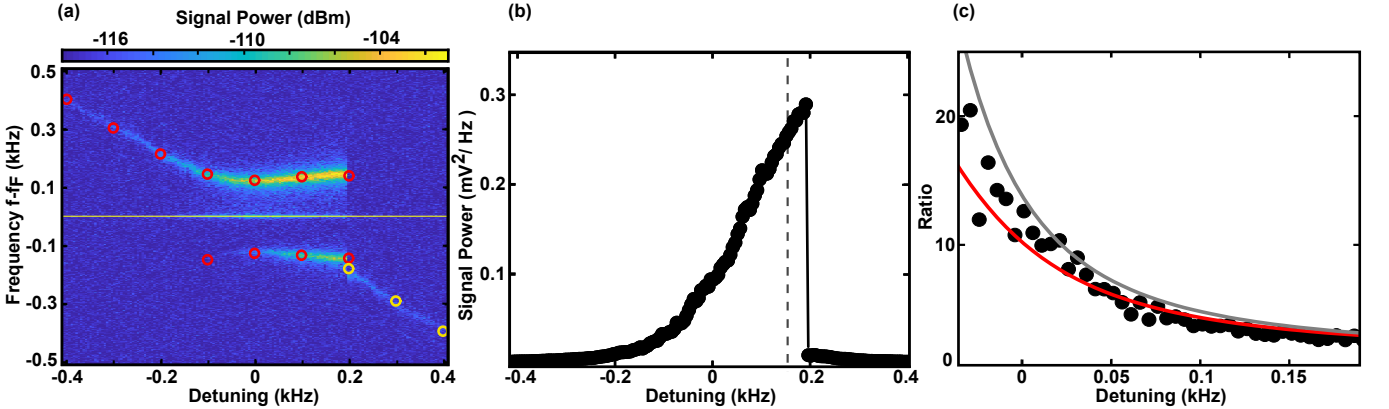


Figure 3. (a), Color coded power spectra showing the positions and intensities of the satellite peaks as a function of the detuning of the drive frequency $f_F - f_0$ for the drive power -20 dBm. The central line at $f - f_F = 0$ is plotted with a reduced brightness to improve the visibility of the satellites. Open circles denote the calculated positions for the high (red) and low (yellow) amplitude states (see Fig. 1b). (b) The power of the signal at the drive frequency f_F as a function of the detuning. The discontinuity observed at a detuning of 190 Hz indicates the switching of the resonator from the high- to the low-amplitude state for a slow ramp up of the detuning. It coincides with the discontinuity of the satellite peaks in Fig. 3a. Dashed gray line indicates the theoretically calculated critical switching point. (c) Ratio of the areas of the satellite peaks for the high-amplitude state as a function of the detuning. Red and gray lines show the theoretical predictions with and without the account taken of the weak overlapping of the satellite peaks, respectively.

This allows the resonator to approach its most probable stable state for every applied detuning and clearly demonstrates sharp switching between occupying practically one or the other state.

The switching point observed in Fig. 3b is expected to be close to the theoretical critical switching point, which is shown by a dashed gray line ($V_{in} = 65$ mV). Indeed, the difference between the experimental and theoretical values is only 40 Hz. This difference can be attributed to a slight non-adiabaticity of the frequency sweep. Furthermore, given the statistical nature of the switching, slow room temperature fluctuations cannot be ruled out as an alternative source of the discrepancy, because the effect of a typical eigenfrequency drift of almost 1 kHz/K could not be completely eliminated, even though the eigenfrequency was re-determined prior to every measurement. In the future, the results can be extended to measure the individual switching rates using different sweep times [49–51].

We emphasize that, in the regime we have studied, the driven resonator has no detailed balance. Understanding fluctuation-induced transitions between the stable states of systems lacking detailed balance, i.e., generically, for all systems away from thermal equilibrium, is of interest for various areas of physics, chemistry, and biology. The weak-damping regime attained in the present work is particularly important, as the phase space of the system is two-dimensional rather than the effectively one-dimensional phase space close to bifurcation points. A high-dimensional phase space significantly complicates the theoretical analysis of the switching rate. To the best of our knowledge, the present results show the first quantitative comparison with analytical results obtained for systems lacking detailed balance.

VIII. CONCLUSIONS

In conclusion, we report the direct observation of classical thermal squeezing using the power spectrum of a vibrational mode. An experimentally much more involved homodyne measurement is not required. The power spectrum of the nanomechanical resonator that we studied exhibits two perfectly resolved satellite peaks symmetrically positioned with respect to the drive frequency. They originate from the thermally induced small-amplitude vibrations about the stable state of forced vibrations, and can be thought of as Stokes and anti-Stokes component in a Raman scattering picture with the caveat that the underlying process is multi-photon, as multiple photons of the resonant driving field are involved.

The satellite peaks feature unequal intensities. The ratio of the intensities is determined by the squeezing parameter. It was directly read out from the experimental data. Our findings are supported by a theoretical model which is in excellent agreement with the experimental data with no free parameters. The model shows that, for the resonantly driven underdamped Duffing resonator, the squeezed quadrature can be suppressed by a factor of 2, giving rise to a 3 dB limit, as in the case of parametrically induced squeezing [16]. Importantly, no fine tuning to a specific operation point is required for obtaining squeezing in a high- Q resonator.

Squeezing of classical fluctuations about the state of forced vibrations in weakly damped nonlinear systems is a generic concept, as it is related to the breaking of the continuous time translation symmetry by the drive. Weakly damped vibrational modes are broadly used in various areas, and squeezing is of major interest for

numerous applications, in particular in high-sensitivity measurements. A promising application is the possibility of employing driven weakly damped modes as detectors of weak signals at frequency f_S close to the drive frequency, $|f_F - f_S| \approx \omega_j$, at room temperature. Associated with the squeezing is the possibility to resonantly amplify such signals, which can be thought of as a multi-photon analog of stimulated Raman scattering, a phenomenon that has not yet been studied in the experiment.

Our results provide an experimental basis for detecting squeezing not only of classical, but also of quantum fluctuations. By extending the analysis [27] we expect such squeezing to occur for a resonantly driven Duffing resonator in spite of the quantum heating effect observed

for such a system [52].

IX. ACKNOWLEDGEMENTS

Financial support by the Deutsche Forschungsgemeinschaft via the collaborative research center SFB 767, the European Unions Horizon 2020 Research and Innovation Programme under Grant Agreement No 732894 (FET Proactive HOT), and the German Federal Ministry of Education and Research (contract no. 13N14777) within the European QuantERA cofund project QuaSeRT is gratefully acknowledged. M. I. D. also acknowledges support from the Zukunftskolleg Senior Fellowship at the University of Konstanz and from the National Science Foundation (Grant No. DMR-1806473). Data and analysis code are available at XXX.

[1] D. F. Walls, *Squeezed states of light*, *Nature* **306**, 141 (1983).

[2] D. F. Walls and G. J. Milburn, *Quantum Optics* (Springer, Berlin, 2008).

[3] R. E. Slusher, L. W. Hollberg, B. Yurke, J. C. Mertz, and J. F. Valley, *Observation of Squeezed States Generated by Four-Wave Mixing in an Optical Cavity*, *Physical Review Letters* **55**, 2409 (1985).

[4] E. E. Wollman, C. U. Lei, A. J. Weinstein, J. Suh, A. Kronwald, F. Marquardt, A. A. Clerk, and K. C. Schwab, *Quantum squeezing of motion in a mechanical resonator*, *Science* **349**, 952 (2015).

[5] F. Lecocq, J. B. Clark, R. W. Simmonds, J. Aumentado, and J. D. Teufel, *Quantum Nondemolition Measurement of a Nonclassical State of a Massive Object*, *Physical Review X* **5**, 041037 (2015).

[6] J.-M. Pirkkalainen, E. Damskägg, M. Brandt, F. Massel, and M. A. Sillanpää, *Squeezing of Quantum Noise of Motion in a Micromechanical Resonator*, *Physical Review Letters* **115**, 243601 (2015).

[7] C. M. Caves, *Quantum-mechanical noise in an interferometer*, *Physical Review D* **23**, 1693 (1981).

[8] J. Aasi *et al.*, *Enhanced sensitivity of the LIGO gravitational wave detector by using squeezed states of light*, *Nature Photonics* **7**, 613 (2013).

[9] M. Malnou, D. A. Palken, B. M. Brubaker, L. R. Vale, G. C. Hilton, and K. W. Lehnert, *Squeezed Vacuum Used to Accelerate the Search for a Weak Classical Signal*, *Physical Review X* **9**, 021023 (2019).

[10] J. Klaers, *Landauer's Erasure Principle in a Squeezed Thermal Memory*, *Physical Review Letters* **122**, 040602 (2019).

[11] F. DiFilippo, V. Natarajan, K. R. Boyce, and D. E. Pritchard, *Classical amplitude squeezing for precision measurements*, *Physical Review Letters* **68**, 2859 (1992).

[12] V. Natarajan, F. DiFilippo, and D. E. Pritchard, *Classical Squeezing of an Oscillator for Subthermal Noise Operation*, *Physical Review Letters* **74**, 2855 (1995).

[13] A. Szorkovszky, G. A. Brawley, A. C. Doherty, and W. P. Bowen, *Strong Thermomechanical Squeezing via Weak Measurement*, *Physical Review Letters* **110**, 184301 (2013).

[14] B. Yurke, P. G. Kaminsky, R. E. Miller, E. A. Whitaker, A. D. Smith, A. H. Silver, and R. W. Simon, *Observation of 4.2-K equilibrium-noise squeezing via a Josephson-parametric amplifier*, *Physical Review Letters* **60**, 764 (1988).

[15] B. Yurke, L. R. Corruccini, P. G. Kaminsky, L. W. Rupp, A. D. Smith, A. H. Silver, R. W. Simon, and E. A. Whitaker, *Observation of parametric amplification and deamplification in a Josephson parametric amplifier*, *Physical Review A* **39**, 2519 (1989).

[16] D. Rugar and P. Grütter, *Mechanical parametric amplification and thermomechanical noise squeezing*, *Physical Review Letters* **67**, 699 (1991).

[17] D. W. Carr, S. Evoy, L. Sekaric, H. G. Craighead, and J. M. Parpia, *Parametric amplification in a torsional microresonator*, *Applied Physics Letters* **77**, 1545 (2000).

[18] J. Suh, M. D. LaHaye, P. M. Echternach, K. C. Schwab, and M. L. Roukes, *Parametric amplification and back-action noise squeezing by a qubit-coupled nanoresonator*, *Nano Letters* **10**, 3990 (2010).

[19] A. Vinante and P. Falferi, *Feedback-Enhanced Parametric Squeezing of Mechanical Motion*, *Physical Review Letters* **111**, 207203 (2013).

[20] M. Poot, K. Y. Fong, and H. X. Tang, *Classical non-Gaussian state preparation through squeezing in an optoelectromechanical resonator*, *Physical Review A* **90**, 063809 (2014).

[21] S. Sonar, V. Fedoseev, M. J. Weaver, F. Luna, E. Vlieg, H. van der Meer, D. Bouwmeester, and W. Löfller, *Strong thermomechanical squeezing in a far-detuned membrane-in-the-middle system*, *Physical Review A* **98**, 013804 (2018).

[22] I. Mahboob, H. Okamoto, K. Onomitsu, and H. Yamaguchi, *Two-Mode Thermal-Noise Squeezing in an Electromechanical Resonator*, *Physical Review Letters* **113**, 167203 (2014).

[23] Y. S. Patil, S. Chakram, L. Chang, and M. Vengalattore, *Thermomechanical Two-Mode Squeezing in an Ultrahigh-Q Membrane Resonator*, *Physical Review Letters* **115**, 017202 (2015).

[24] A. Pontin, M. Bonaldi, A. Borrielli, L. Marconi, F. Marino, G. Pandraud, G. A. Prodi, P. M. Sarro, E. Serra, and F. Marin, *Dynamical Two-Mode Squeezing of Thermal Fluctuations in a Cavity Optomechanical System*, *Physical Review Letters* **116**, 103601 (2016).

[25] M. I. Dykman and M. A. Krivoglaz, *Theory of fluctuational transitions between stable states of a non linear oscillator*, *Soviet Physics JETP* **50**, 30 (1979).

[26] P. D. Drummond and D. F. Walls, *Quantum-theory of optical bistability. 1: Non-linear polarizability model*, *Journal of Physics A* **13**, 725 (1980).

[27] M. I. Dykman, *Periodically modulated quantum nonlinear oscillators*, in *Fluctuating Nonlinear Oscillators: from Nanomechanics to Quantum Superconducting Circuits*, edited by M. I. Dykman (Oxford University Press, 2012) pp. 165–197.

[28] S. André, L. Guo, V. Peano, M. Marthaler, and G. Schön, *Emission spectrum of the driven nonlinear oscillator*, *Physics Review A* **85**, 053825 (2012).

[29] R. Almog, S. Zaitsev, O. Shtempluck, and E. Buks, *Noise Squeezing in a Nanomechanical Duffing Resonator*, *Physical Review Letters* **98**, 078103 (2007).

[30] M. I. Dykman, M. Marthaler, and V. Peano, *Quantum heating of a parametrically modulated oscillator: Spectral signatures*, *Physics Review A* **83**, 052115 (2011).

[31] C. Stambaugh and H. B. Chan, *Supernarrow Spectral Peaks near a Kinetic Phase Transition in a Driven Nonlinear Micromechanical Oscillator*, *Physical Review Letters* **97**, 110602 (2006).

[32] M. I. Dykman, D. G. Luchinsky, R. Mannella, P. V. E. McClintock, N. D. Stein, and N. G. Stocks, *Supernarrow spectral peaks and high-frequency stochastic resonance in systems with coexisting periodic attractors*, *Physical Review E* **49**, 1198 (1994).

[33] R. Bonifacio and L. A. Lugiato, *Photon statistics and spectrum of transmitted light in optical bistability*, *Physics Review Letters* **40**, 1023 (1978).

[34] See Supplemental Material at **(URL given by editor)** for the theoretical analysis of the thermal noise squeezing and its relation with power spectrum in a driven Duffing resonator, the characterisation of the nanobeam resonator, the calibration of the detection setup, the analysis of the data and further supplementary experimental data.

[35] T. Faust, P. Krenn, S. Manus, J. P. Kotthaus, and E. M. Weig, *Microwave cavity-enhanced transduction for plug and play nanomechanics at room temperature*, *Nature Communications* **3**, 728 (2012).

[36] Q. P. Unterreithmeier, T. Faust, and J. P. Kotthaus, *Damping of Nanomechanical Resonators*, *Physics Review Letters* **105**, 027205 (2010).

[37] M. Gad-el Hak, *The MEMS Handbook* (CRC, Press, 2002).

[38] S. S. Verbridge, J. M. Parpia, R. B. Reichenbach, L. M. Bellan, and H. G. Craighead, *High quality factor resonance at room temperature with nanostrings under high tensile stress*, *Journal of Applied Physics* **99**, 124304 (2006).

[39] Q. P. Unterreithmeier, E. M. Weig, and J. P. Kotthaus, *Universal transduction scheme for nanomechanical systems based on dielectric forces*, *Nature* **458**, 1001 (2009).

[40] J. Rieger, T. Faust, M. J. Seitner, J. P. Kotthaus, and E. M. Weig, *Frequency and Q factor control of nanomechanical resonators*, *Applied Physics Letters* **101**, 103110 (2012).

[41] L. D. Landau and E. M. Lifshitz, *Theory of Elasticity (Volume 7 of A Course of Theoretical Physics)* (Pergamon, 1970).

[42] A. H. Nayfeh and D. T. Mook, *Nonlinear oscillations*, 7th ed. (Wiley, 1995).

[43] M. Dykman, *Fluctuating Nonlinear Oscillators: From Nanomechanics to Quantum Superconducting Circuits*, 1st ed. (Oxford University Press, 2012).

[44] M. I. Dykman and M. A. Krivoglaz, *Theory of Nonlinear Oscillators Interacting with a Medium*, in *Sov. Phys. Reviews*, Vol. 5, edited by I. M. Khalatnikov (Harwood Academic, New York, 1984) pp. 265–441, web.pa.msu.edu/dykman/pub06/DKreview84.pdf.

[45] M. I. Dykman and M. A. Krivoglaz, *Classical theory of nonlinear oscillators interacting with a medium*, *Physica Status Solidi B* **48**, 497 (1971).

[46] M. Pernpeintner, T. Faust, F. Hocke, J. P. Kotthaus, E. M. Weig, H. Huebl, and R. Gross, *Circuit electromechanics with a non-metallized nanobeam*, *Applied Physics Letters* **105**, 123106 (2014).

[47] V. I. Arnold, *Mathematical Methods of Classical Mechanics* (Springer, New York, 1989).

[48] V. Peano and M. Thorwart, *Quasienergy description of the driven Jaynes-Cummings model*, *Physics Review B* **82**, 155129 (2010).

[49] J. S. Aldridge and A. N. Cleland, *Noise-Enabled Precision Measurements of a Duffing Nanomechanical Resonator*, *Physics Review Letters* **94**, 156403 (2005).

[50] C. Stambaugh and H. B. Chan, *Noise-activated switching in a driven nonlinear micromechanical oscillator*, *Physics Review B* **73**, 172302 (2006).

[51] M. Defoort, V. Puller, O. Bourgeois, F. Pistolesi, and E. Collin, *Scaling laws for the bifurcation escape rate in a nanomechanical resonator*, *Physics Review E* **92**, 050903 (2015).

[52] F. R. Ong, M. Boissonneault, F. Mallet, A. C. Doherty, A. Blais, D. Vion, D. Esteve, and P. Bertet, *Quantum Heating of a Nonlinear Resonator Probed by a Superconducting Qubit*, *Physics Review Letters* **110**, 047001 (2013).

Supplemental Material: Detecting squeezing from the fluctuation spectrum of a driven nanomechanical mode

J. S. Huber,¹ G. Rastelli,¹ M. J. Seitner,¹ J. Kölbl,^{1,*} W. Belzig,¹ M. I. Dykman,² and E. M. Weig¹

¹*Department of Physics, University of Konstanz, 78457 Konstanz, Germany*

²*Michigan State University, East Lansing, MI 48824, USA*

In this Supplemental Material we provide the theoretical analysis of the thermal noise squeezing and its relation with power spectrum in a driven Duffing resonator, the characterisation of the nanomechanical resonator, the calibration of the detection setup, the analysis of the data presented in the main text and further supplementary experimental data.

I. THEORY

A. The Duffing model

The fundamental mode of the silicon nitride nanostring resonator under investigation is well described by the model of the Duffing resonator. The beam displacement q at the antinode follows the equation

$$\ddot{q} + 2\Gamma\dot{q} + \omega_0^2 q + \gamma q^3 = F \cos(\omega_F t) + \xi(t), \quad (\text{S1})$$

in which Γ is the damping coefficient, ω_0 is the mode eigenfrequency, γ is the Duffing nonlinearity parameter, F is the amplitude of the external driving, and ω_F is the driving frequency. In our experiment we have $\gamma > 0$. The vibrations have inversion symmetry, and therefore there is no term $\propto q^2$ in Eq. (S1). Here for brevity we have set the effective mass of the resonator at the position of the antinode $m = 1$; alternatively, one can think that the forces F and $\xi(t)$ incorporate the factor $1/m$.

The term $\xi(t)$ represents the thermal noise. Since the frequency ω_0 is small compared to $k_B T/\hbar$ and compared to the reciprocal correlation time of the thermal reservoir (thermal phonons, in our system), the dissipation has no delay and the noise $\xi(t)$ is zero-mean, Gaussian, and δ -correlated. With the effective mass taken explicitly into account, the noise correlator reads $\langle \xi(t) \rangle = 0$ and $\langle \xi(t) \xi(t') \rangle = \delta(t - t') 4\Gamma k_B T/m$, where T is the room temperature.

It is convenient to switch to the rotating frame and to introduce the scaled complex vibration amplitude v ,

$$q(t) = \sqrt{\frac{2\omega_F \Gamma}{3\gamma}} [v(t)e^{i\omega_F t} + v^*(t)e^{-i\omega_F t}], \quad \dot{q}(t) = \sqrt{\frac{2\omega_F \Gamma}{3\gamma}} (i\omega_F) [v(t)e^{i\omega_F t} - v^*(t)e^{-i\omega_F t}]. \quad (\text{S2})$$

The relations with the two quadratures defined in the main text are simply $x_1 = \sqrt{8\omega_F \Gamma/(3\gamma)} \operatorname{Re} v$ and $x_2 = -\sqrt{8\omega_F \Gamma/(3\gamma)} \operatorname{Im} v$. In the rotating wave approximation (RWA), we obtain from Eq. (S1) the equation of motion for $v(t)$ in the form

$$\dot{v} = i \frac{\partial h_v}{\partial v^*} - \Gamma v - i\Gamma \xi_v(t); \quad h_v = \Gamma \left[\frac{1}{2} |v|^4 - \Omega |v|^2 - \beta_v^{1/2} (v + v^*) \right]. \quad (\text{S3})$$

Here $\Omega = \delta\omega/\Gamma$, with $\delta\omega = \omega_F - \omega_0$ being the frequency detuning of the drive from the mode eigenfrequency; it is assumed to be small for resonant driving, $\omega_0, \omega_F \gg |\delta\omega|$. Parameter β_v is the scaled driving strength and $\xi_v(t)$ is Gaussian noise,

$$\beta_v = \frac{3\gamma F^2}{32\omega_F^3 \Gamma^3}, \quad \xi_v = \sqrt{\frac{3\gamma}{8\omega_F^3 \Gamma^3}} \xi(t) e^{-i\omega_F t}, \quad \langle \xi_v(t) \xi_v^*(t') \rangle = \frac{4\alpha}{\Gamma} \delta(t - t'), \quad \alpha = \frac{3\gamma k_B T}{8\omega_F^3 \Gamma}. \quad (\text{S4})$$

The evolution of $v(t)$ occurs slowly, on a timescale of $\sim \Gamma^{-1}$. On such timescale the correlator $\langle \xi_v(t) \xi_v^*(t') \rangle$, which is fast oscillating in time, can be disregarded, i.e., $\xi_v(t)$ is correlated only with $\xi_v^*(t)$. The function h_v is the scaled Hamiltonian h introduced in Eq. (4) of the main text, see also Fig. 1c.

In the absence of noise, the stationary solutions of Eq. (S3) give the scaled complex amplitude of forced vibrations v_j , where j enumerates the solutions,

$$v_j = -\frac{i\beta_v^{1/2}}{1 + i\Omega - i|v_j|^2}, \quad (\text{S5})$$

* Department of Physics, University of Basel, 4056 Basel, Switzerland

or

$$\phi_v(|v_j|^2) = 0, \quad \phi_v(x) = x [1 + (x - \Omega)^2] - \beta_v \quad (S6)$$

The cubic equation $\phi_v(|v_j|^2) = 0$ can have three real roots. This occurs in the region of vibration bistability, which is bounded by the bifurcational values of the dimensional parameter β_v

$$(\beta_v)_{B1,2} = \frac{2}{27} [\Omega(\Omega^2 + 9) \pm (\Omega^2 - 3)^{3/2}]. \quad (S7)$$

The smallest and the largest roots $|v_j|^2$ correspond to the stable vibrational states of the driven mode (denoted in the main text by l_0 and h_i , respectively), the intermediate root corresponds to an unstable stationary state. The squared resonator amplitudes are $A_j^2 = (8\omega_F\Gamma/3\gamma)^{1/2}|v_j|^2$ with $j = h_i, l_0$. An example of the dependence of A_j on the drive frequency is shown as the response function in Fig. 1b of the main text.

B. Linearized dynamics

The noise leads to fluctuations of the driven resonator. For weak noise the major effects are small-amplitude fluctuations about the stable vibrational states and rare events where the noise causes transitions between the states [S1]. A simple approach to the analysis of the small-amplitude fluctuations is based on linearizing the equation of motion Eq. (S3) about the stable vibrations states [S1–S3]. The linearized equations for $\delta v_j(t) = v(t) - v_j$ read

$$\delta \dot{v}_j(t) = -\Gamma \left(1 + i\Omega - 2i|v_j|^2 \right) \delta v_j + i\Gamma v_j^2 \delta v_j^* - i\Gamma \xi_v. \quad (S8)$$

The dynamics of $\delta v_j(t)$ is similar to the dynamics of a linear damped harmonic oscillator subject to noise. The characteristic frequency scale of the fluctuations is determined by the eigenvalue of Eq. (S8) $\Gamma v_{v,j}$,

$$v_{v,j}^2 = \left(3|v_j|^2 - \Omega \right) \left(|v_j|^2 - \Omega \right) + 1 = (\omega_j/\Gamma)^2 + 1 \quad (S9)$$

with ω_j given by Eq. (5) of the main text. We note that $v_{v,j} \approx \omega_j/\Gamma$ for $\omega_j \gg \Gamma$.

C. The power spectrum

Fluctuations of the complex amplitude $v(t)$ lead to fluctuations of the coordinate $q(t)$ of the nanoresonator. Such fluctuations are of considerable broad interest, given that the driven nanomechanical resonator is a system far away from thermal equilibrium. They can be directly measured in the experiment by measuring the power spectrum of the nanoresonator. For the periodically driven nanoresonator the power spectrum is defined as

$$\begin{aligned} Q(\omega) &= \frac{1}{\pi} \text{Re} \int_0^\infty dt e^{i\omega t} \bar{Q}(t), \\ \bar{Q}(t) &= \frac{\omega_F}{2\pi} \int_0^{2\pi/\omega_F} dt' [\langle q(t+t')q(t') \rangle - \langle q(t+t') \rangle \langle q(t') \rangle]. \end{aligned} \quad (S10)$$

Since the dynamics of the nanoresonator is mostly oscillations at frequency ω_F with the amplitude and phase that vary slowly over time $\sim 1/\omega_F$, the spectrum $Q(\omega)$ has peaks centered in a range $\sim |\delta\omega|, \Gamma$ around the drive frequency ω_F (and $-\omega_F$, strictly speaking).

Near ω_F the spectrum $Q(\omega)$ is given by the power spectrum of the complex amplitude $v(t)$, as seen from Eq. (S2),

$$Q(\omega) \approx \frac{2\omega_F\Gamma}{3\pi\gamma} \text{Re} \int_0^\infty dt e^{i(\omega-\omega_F)t} \langle [v^*(t) - \langle v^* \rangle] [v(0) - \langle v \rangle] \rangle. \quad (S11)$$

In the range of bistability, $\langle v \rangle$ is approximately the sum of the values v_{h_i, l_0} weighted with the mean occupation of the corresponding states. For weak noise, these occupations are of the same order of magnitude only in a very narrow parameter range (the region of the kinetic phase transition [S1]). Away from this region only one of the stable states is mostly occupied. Also, if the

measurement is done over a time which is small compared to the reciprocal rate of interstate transitions, $\langle v \rangle$ should be replaced by the value v_j in the state in which the system was prepared. Then $Q(\omega)$ is given by the partial spectrum

$$Q_j(\omega) = \frac{2\omega_F\Gamma}{3\pi\gamma} \operatorname{Re} \int_0^\infty dt e^{i(\omega-\omega_F)t} \langle \delta v_j^*(t) \delta v_j(0) \rangle. \quad (\text{S12})$$

For a long observation time, in addition to the partial spectra given by Eq. (S12) the full spectrum $Q(\omega)$ displays an extremely narrow peak in the region of the kinetic phase transition [S3], which has been seen in micromechanical resonators driven by a noise that imitated a relatively high-temperature thermal noise [S4]. In this work we do not consider this peak, since our primary interest focuses on the spectra $Q_j(\omega)$.

Calculating $Q_j(\omega)$ in the region where the motion around the stable states can be linearized and is described by Eq. (S8) is straightforward, [S2, S3], giving

$$Q_j(\omega) = \frac{\Gamma k_B T}{2\pi\omega_F^2} \frac{\left(\omega - \omega_F + 2\Gamma|v_j|^2 - \delta\omega\right)^2 + \Gamma^2 \left(1 + |v_j|^4\right)}{\left[(\omega - \omega_F)^2 - \Gamma^2 v_{v,j}^2\right]^2 + 4\Gamma^2(\omega - \omega_F)^2}. \quad (\text{S13})$$

The total area of the power spectrum Eq. (S13) is

$$I_j \equiv \int d\omega Q_j(\omega) = \frac{k_B T}{2\omega_F^2} \left[1 + \frac{|v_j|^4}{v_{v,j}^2} \right]. \quad (\text{S14})$$

This area exceeds the area of the power spectrum in the absence of the drive, which is given by the above expression with $|v_j|^2$ set equal to zero. Therefore it turned out to be possible to observe the satellite peaks of the power spectrum of the driven resonator even where in the absence of the driving the resolution of the experiment did not allow us to reliably detect the power spectrum.

For the discussion of the squeezing effect it is convenient to consider the areas of the power spectrum for $\omega > \omega_F$ and for $\omega < \omega_F$, which we denote as $I_j^{(+)}$ and $I_j^{(-)}$, respectively. They have the form

$$I_j^{(\pm)} = \frac{1}{2} I_j \pm \Delta I_j, \quad \Delta I_j = \frac{k_B T}{2\pi\omega_F^2} \frac{2|v_j|^2 - \Omega}{\sqrt{v_{v,j}^2 - 1}} \arctan \left(\sqrt{v_{v,j}^2 - 1} \right). \quad (\text{S15})$$

This expression can be analytically continued in a standard way to the region $v_{v,j} < 1$. The definition of the areas in Eq. (S15) takes into account the overlapping, for not too large v_j , of the satellite peaks centered at $\approx \pm\Gamma v_j$. This analytic expression is used in the comparison with the experiment in Figs. 2 and 3 of the main text.

The results for the two areas of Eq. (S15) are shown in Fig. S1 for the high amplitude state. Here we compare these analytic results with the results of the following procedure, which is also the procedure used to extract the satellite areas from the experimental data. The power spectrum $Q_j(\omega)$, Eq. (S13), is fit by two Lorentzians, with the maxima in the regions $\omega > \omega_F$ and $\omega < \omega_F$, respectively. The areas of the satellite peaks is then found from the parameters of the Lorentzians. Figure S1a and b display these areas as a function of the scaled driving strength β_v and the scaled detuning $\delta\omega_F/\Gamma$, respectively. The upper x -axis converts these values into the real drive power and detuning, for the parameters of the nanomechanical resonator studied in the experiment. The parameters are chosen to match those discussed in Figs. 2b and c, as well as Fig. 3c of the main text. There is a good agreement between the areas of the satellite peaks found from the Lorentzian fits and the areas of the parts of the analytical spectrum at $\omega > \omega_F$ and $\omega < \omega_F$ given by Eq. (S15).

D. Squeezed thermal fluctuations for weak damping

The power spectrum $Q_j(\omega)$ has a particularly simple form in the case of weak damping, where $v_{v,j} \gg 1$. Here $Q_j(\omega)$ has two distinct, non-overlapping satellite peaks at frequencies $\omega_F \pm \Gamma v_{v,j}$. Similar peaks emerge in the response of the resonator to an extra drive [S1]. It should be emphasized that the weak-damping condition implied here is much stronger than the condition $\Gamma \ll \omega_0$ of the nanoresonator to be underdamped. The advantageous feature of the resonator studied in this work is that both conditions are met in the experiment, in a certain range of the amplitude and frequency of the driving field.

To analyze the dynamics in the weak-damping limit we re-write Eqs. (S8) separating the terms of the first order in the friction coefficient Γ . From Eq. (S5), to the leading order in Γ we have $v_j^2 \approx \bar{v}_j^2$ with a real positive ($\bar{v}_j^2 \propto \Gamma^{-1}$) given by Eq. (S16) below, to the first order in Γ

$$v_j \approx \bar{v}_j \left(1 - \frac{i}{\bar{v}_j^2 - \Omega} \right), \quad \bar{v}_j^2 \left(\bar{v}_j^2 - \Omega \right)^2 = \beta_v. \quad (\text{S16})$$

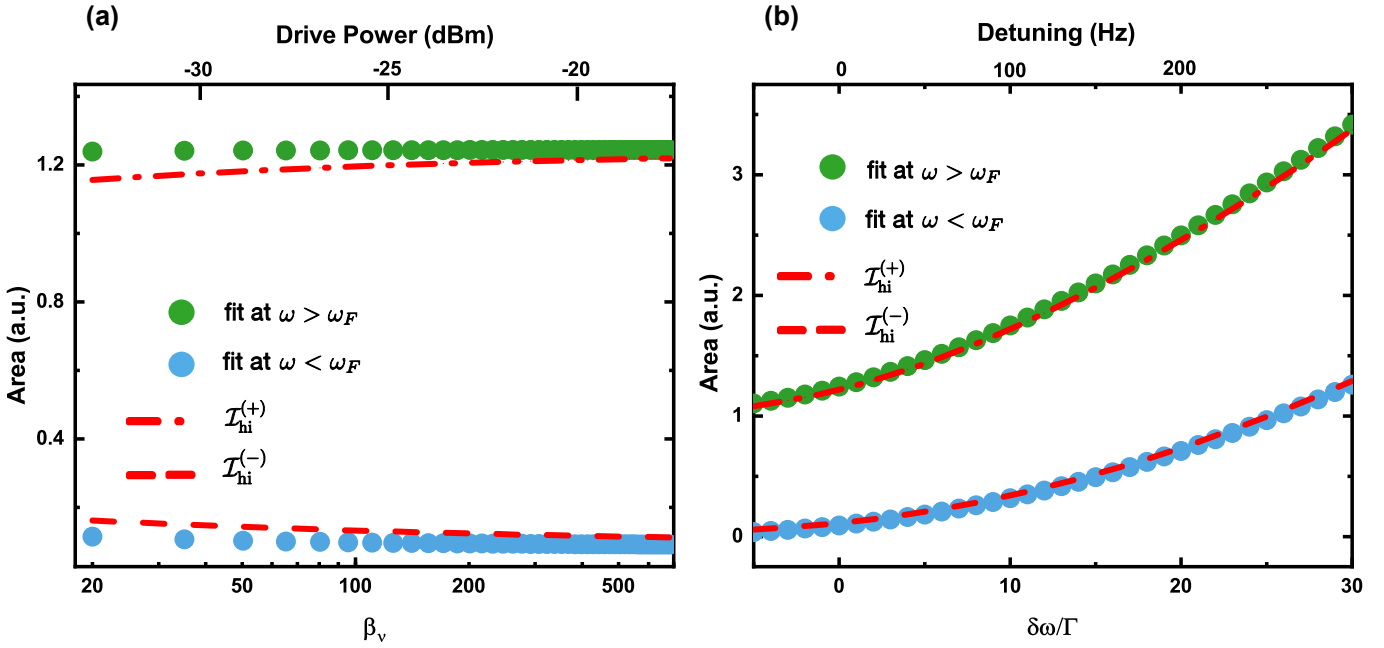


Figure S1. The red dash-dotted and dashed lines show the integrals of Eq. (S15) for the high amplitude state, $\mathcal{I}_{\text{hi}}^{(+)}$ and $\mathcal{I}_{\text{hi}}^{(-)}$, respectively. The integrals are scaled by $k_B T / (2\omega_F^2)$. The green and blue dots are obtained by fitting the power spectrum $Q_{\text{hi}}(\omega)$ of Eq. (S13) (scaled by $k_B T / (2\omega_F^2)$) by two Lorentzians centered at the maxima of $Q_{\text{hi}}(\omega)$. **a** Comparison as a function of scaled driving strength β_v at zero detuning $\delta\omega_F = 0$. **b** Comparison as a function of scaled detuning $\delta\omega_F/\Gamma$ at $\beta_v = 700$.

Equations (S8) for the small deviations $\delta v_j, \delta v_j^*$ from the stable states can be written as

$$\delta \dot{v}_j = i \frac{\partial \delta h_j}{\partial \delta v_j^*} - \Gamma(\delta v_j + \mu_j \delta v_j^*) - i\Gamma \xi_v(t), \quad \delta h_j = \Gamma(2\bar{v}_j^2 - \Omega) |\delta v_j|^2 + \frac{1}{2} \bar{v}_j^2 \left[(\delta v_j^*)^2 + \delta v_j^2 \right]. \quad (\text{S17})$$

Here, the Hamiltonian δh_j is the expansion of the Hamiltonian h_v , Eq. (S3), about \bar{v}_j to the second order in $\delta v_j, \delta v_j^*$. Parameter $\mu_j = 2\bar{v}_j^2 / (\bar{v}_j^2 - \Omega)$ was introduced in the main text. It should be noted that the phase of the scaled complex amplitude v_j in a stable state j is “pinned” to the phase of the driving field. This phase directly reflects the broken time-translation symmetry of the stable state. The Hamiltonian δh_j thus also “knows” about the phase of the field. This leads to the terms $\propto (\delta v_j)^2, (\delta v_j^*)^2$. If there were no such terms, the quadratures of the fluctuations about the stable state would be equal (we recall that these quadratures are given by the scaled $\text{Re } \delta v_j$ and $-\text{Im } \delta v_j$, respectively). Indeed, as seen from the expression for the correlators $\xi_v(t)$, in this case we would have $\langle \delta v_j^2 \rangle = \langle (\delta v_j^*)^2 \rangle = 0$. However, the latter expression does not apply to our driven nonlinear resonator.

Since, as noted above, for weak damping $v_j \propto \Gamma^{-1/2}$ and $\Omega \propto \Gamma^{-1}$, the Hamiltonian δh_j is independent of Γ . This Hamiltonian can be diagonalized by the Bogoliubov (squeezing) transformation

$$\delta v_j = u_j \cosh \varphi_j - u_j^* \sinh \varphi_j, \quad (\text{S18})$$

so that the new Hamiltonian for the variables u_j contains only $|u_j|^2$ and not $u_j^2, (u_j^*)^2$. This condition is met if we set

$$\tanh(2\varphi_j) = \frac{\bar{v}_j^2}{2\bar{v}_j^2 - \Omega}. \quad (\text{S19})$$

The resulting equation of motion is

$$\dot{u}_j = i \frac{\partial \delta h_j}{\partial u_j^*} - \Gamma u_j - \Gamma \mu_j u_j^* - i\Gamma \xi_j(t), \quad \delta h_j = \Theta_j \Gamma v_{v,j} |u_j|^2, \quad \Theta_j = \text{sgn}(2\bar{v}_j^2 - \Omega), \quad \xi_j(t) = \xi_v(t) \cosh \varphi_j - \xi_v^*(t) \sinh \varphi_j. \quad (\text{S20})$$

In this expression only the leading-order term with respect to Γ should be taken into account in $v_{v,j}$, i.e., $v_{v,j} = [(3\bar{v}_j^2 - \Omega)(\bar{v}_j^2 - \Omega)]^{1/2}$. Clearly, $\Gamma v_{v,j}$ is independent of Γ . The coefficient $\Theta_j = \pm 1$ is given by the sign of $2\bar{v}_j^2 - \Omega$. Parameter φ_j is simply related to the standard [S5] parameters (r, θ) of the squeezing transformation: $r = \varphi_j, \theta = 0$ for $\Theta_j = 1$, and $r = |\varphi_j|, \theta = \pi$ for $\Theta_j = -1$.

To the lowest order in Γ , the variable u_j is oscillating as $\exp[i\Theta_j\Gamma\nu_{v,j}t]$. The coefficient Θ_j reflects the fact that, in the range of bistability, u_j is rotating in the opposite directions for the large and small amplitude stable states where, as it is well-known for the Duffing resonator, $2\bar{v}_j^2 - \Omega$ is positive or negative, respectively. Function $u_j^*(t)$ is rotating in the direction opposite to $u_j(t)$. Therefore, for small Γ (or equivalently, for $\nu_{v,j} \gg 1$), the term $\propto \mu_j$ in Eq. (S20) can be disregarded. Then, using the Stratonovich convention for averaging δ -correlated noise, we see from Eqs. (S4) and (S20) that

$$\langle |u_j|^2 \rangle \approx 2\alpha \cosh 2\varphi_j, \quad (S21)$$

whereas the mean value $\langle u_j^2 \rangle \approx -i(2\alpha/\nu_{v,j}) \sinh 2\varphi_j$ is much smaller and can be disregarded. As a result we have for the average values of the quadratures

$$\langle (\text{Re } \delta v_j)^2 \rangle \approx \frac{\alpha}{2} (1 + e^{-4\varphi_j}), \quad \langle (\text{Im } \delta v_j)^2 \rangle \approx \frac{\alpha}{2} (1 + e^{4\varphi_j}), \quad (S22)$$

which demonstrates the squeezing of thermal fluctuations about the stable state of forced vibrations. Going back to the unscaled quadratures x_1, x_2 , Eq. (S22) gives

$$\langle \delta x_1^2 \rangle = \frac{k_B T}{2\omega_F^2} (1 + e^{-4\varphi_j}), \quad \langle \delta x_2^2 \rangle = \frac{k_B T}{2\omega_F^2} (1 + e^{4\varphi_j}). \quad (S23)$$

Equation (S20) for u_j has a simple solution

$$u_j(t) = \exp[-(\Gamma - i\Theta_j\Gamma\nu_{v,j})t] \left[u_j(0) - i\Gamma \int_0^t \exp[(\Gamma - i\Theta_j\Gamma\nu_{v,j})t'] \xi_j(t') \right]. \quad (S24)$$

With this solution, using Eqs. (S11) and (S18) we obtain

$$\begin{aligned} Q_j(\omega) &\approx \frac{\Gamma k_B T}{4\pi\omega_F^2} \frac{\cosh 2\varphi_j (1 + \cosh 2\varphi_j)}{(\omega - \omega_F - \Theta_j\Gamma\nu_{v,j})^2 + \Gamma^2}, \quad |\omega - \omega_F - \Theta_j\Gamma\nu_{v,j}| \ll \Gamma\nu_{v,j}, \\ Q_j(\omega) &\approx \frac{\Gamma k_B T}{4\pi\omega_F^2} \frac{\cosh 2\varphi_j (\cosh 2\varphi_j - 1)}{(\omega - \omega_F + \Theta_j\Gamma\nu_{v,j})^2 + \Gamma^2}, \quad |\omega - \omega_F + \Theta_j\Gamma\nu_{v,j}| \ll \Gamma\nu_{v,j}. \end{aligned} \quad (S25)$$

The power spectrum Eq. (S25) coincides with Eq. (11) of the main text if one takes into account that $\Theta_j = 1$ for the high amplitude stable state and $\Theta_j = -1$ for the low amplitude stable state. The spectrum consists of two Lorentzian peaks with half width Γ . The peaks are located at the drive frequency shifted up and down by the frequency of vibrations in the rotating frame about the stable state j . We emphasize that, since we kept only the leading-order terms in the decay rate Γ , Eq. (S25) applies only in the frequency ranges of the peaks.

It is instructive also to compare the areas of the satellite peaks described by Eq. (S25) with Eq. (S15) for the areas of the peaks on the opposite sides of ω_F . From Eq. (S25), the areas of the peaks are

$$\mathcal{I}_j^{(\pm)} = \frac{k_B T}{4\omega_F^2} \cosh 2\varphi_j (\cosh 2\varphi_j \pm 1) = \frac{k_B T}{4\omega_F^2} \left[1 + \frac{\bar{v}_j^4}{\nu_{v,j}} \pm \frac{2\bar{v}_j^2 - \Omega}{\nu_{v,j}} \Theta_j \right]. \quad (S26)$$

One can easily see that this expression coincides with Eq. (S15) if in the latter equation one goes to the limit $\nu_{v,j} \gg 1$ and replaces $|\nu_j|^2$ with \bar{v}_j^2 , which corresponds to keeping the terms of the lowest-order in Γ .

The central feature of the spectrum Eq. (S25) is that the two satellite peaks of $Q_j(\omega)$ have different amplitudes and areas. This is a direct indication of the squeezing of the vibrations about the stable state. Measuring the ratio of the peak heights allows one to directly determine the squeezing parameter φ_j and thus, if we use the conventional notations of quantum optics, the squeezing parameter $r = |\varphi_j|$.

E. Asymmetry of the satellite peaks

In calculating the spectrum $Q_j(\omega)$ in the previous section we expanded the Hamiltonian h_v to second order in $\delta v, \delta v^*$. Disregarding higher-order terms may be inconsistent in the limit of small decay rate Γ . These terms describe the nonlinearity of the vibrations about the stable states in the rotating frame. Such nonlinearity leads to the dependence of the vibration frequency on the vibration amplitude. Thermal fluctuations of the amplitude then translate into thermal fluctuations of the vibration frequency and thus lead to broadening of the satellite peaks. Such broadening is well understood for nonlinear resonators in the absence of strong periodic driving [S6].

A quantum theory of the nonlinearity-induced spectral broadening of the peaks of $Q_j(\omega)$ was discussed in Ref. [S7]. Here we will briefly outline the corresponding classical theory. As indicated in the main text, the amplitude dependence of the vibration frequency comes from the Duffing nonlinearity in the first order of the perturbation theory. More generally, it is well-known from classical mechanics [S8] that the first-order terms in the amplitude dependence of the vibration frequency come from the terms in the Hamiltonian that are nonzero when averaged over the vibration period. In the case of the Duffing resonator the corresponding term is $\gamma q^4/4$ which, for $q = A \cos(\omega_0 t + \phi)$, has the period-averaged value $3\gamma A^4/32$.

In line with the above argument, to find the amplitude dependence of the vibrations in the rotating frame about a j th state one has to do the following steps:

- Expand the full Hamiltonian h_v about \bar{v}_j to the 4th order in $\delta v_j, \delta v_j^*$.
- Express $\delta v, \delta v^*$ in terms of u_j, u_j^*
- Out of all quartic terms in u_j, u_j^* keep only the term $\propto |u_j|^4$, as this is the only term that does not oscillate in the harmonic approximation.

The above routine has to be augmented to allow for the fact that the cubic terms $\delta h_j^{(3)} = \bar{v}_j |\delta v_j|^2 \cdot (\delta v_j + \delta v_j^*)$ will contribute to the amplitude dependence of the frequency when taken to the second order of the perturbation theory. The corresponding terms renormalize the coefficient in front of the term $\propto |u_j|^4$. The result is as if the relevant quartic term in u_j, u_j^* of the effective Hamiltonian has the form

$$\delta h_j^{(4)} = \frac{1}{2} \Gamma B_j |u_j|^4, \quad B_j = \frac{1}{2} \left(3 \cosh^2 2\varphi_j - 1 \right) - \frac{\bar{v}_j^2 \exp(-2\varphi_j)}{\Theta_j v_j} \left(\frac{9}{2} \cosh 4\varphi_j - 3 \sinh 4\varphi_j + \frac{3}{2} \right). \quad (\text{S27})$$

The parameter B_j is determined by the ratio $\beta = \beta_v/\Omega^3$. A plot of $V = 2B_j$ and $v_0 = v_j/\Omega$ as functions of this ratio for the large- and small-amplitude attractor is shown in Fig. 9 of Ref. [S7]. The Hamiltonian $\delta h_j^{(4)}$ has to be added to δh_j in the equation of motion for u_j , Eq. (S20). The resulting equation has the same general form as the equation of motion of an anharmonic Duffing resonator with eigenfrequency $\Gamma\Theta_j v_j$ in the presence of relaxation and noise, but with no driving. Using the results [S7, S9] we can write the power spectrum of the resonator near frequency $\omega_F + \Gamma\Theta_j v_{v,j}$ in the form of a series

$$Q_j(\omega) \approx \frac{k_B T}{4\pi\omega_F^2} \cosh 2\varphi_j (\cosh 2\varphi_j + 1) \operatorname{Re} \sum_n \phi_j(n, \omega - \omega_F - \Gamma\Theta_j v_{v,j}), \quad (\text{S28})$$

$$\phi_j(n, \omega') = \frac{4n(\Lambda_j - 1)^{n-1}(\Lambda_j + 1)^{-(n+1)}}{\Gamma(2\aleph_j n - 1) - i\omega'}. \quad (\text{S29})$$

Here,

$$\Lambda_j = (1 + 2iB_j\alpha \cosh 2\varphi_j)/\aleph_j, \quad \aleph_j = (1 + 4iB_j\alpha \cosh 2\varphi_j)^{1/2} \quad [\operatorname{Re} \aleph_j > 0]. \quad (\text{S30})$$

Near frequency $\omega_F - \Gamma\Theta_j v_j$ the power spectrum has the form

$$Q_j(\omega) \approx \frac{k_B T}{4\pi\omega_F^2} \cosh 2\varphi_j (\cosh 2\varphi_j - 1) \operatorname{Re} \sum_n \phi_j[n, -(\omega - \omega_F + \Gamma\Theta_j v_{v,j})]. \quad (\text{S31})$$

The shape of the spectra in Eqs. (S28) and (S31) is determined by the parameter $B_j\alpha$, i.e., by the effective nonlinearity of the vibrations about the stable vibrational state. If $|B_j|\alpha \ll 1$, the main contribution to the spectra comes from the term $n = 1$ and the spectra are close to the Lorentzian spectra of Eq. (S25). However, if $|B_j|\alpha \gtrsim 1$, the shape of the satellite peaks strongly differs from the Lorentzian shape. Since $|B_j| \sim 1$, the important parameter of the spectral shape is α . This parameter characterizes the ratio of the broadening of the spectrum due to thermal fluctuations of the vibration amplitude and the decay rate. Equations (S28) and (S31) allow one to calculate the shape of the spectrum for an arbitrary α and to see the evolution of the spectrum with increasing α .

We wish to make the following two comments: First, the nonlinearity of the vibrations about the stable states, although it can dramatically change the shape of the peaks at frequencies $\omega_F \pm \Theta_j \Gamma v_{v,j}$ for weak damping, does not change the area of these peaks, to the leading order. Second, it is important to keep in mind that Eq. (S25) applies in the weak damping approximation discussed in section I.D. In this approximation, the decay rate has to be small, so that the satellite peaks described by Eq. (S25) are well resolved. However, it should be not too small if one approximates the shape of the peaks by a Lorentzian.

II. EXPERIMENTAL SETUP, CHARARCTERIZATION AND CALIBRATION

A. Sample and experimental measurement setup

The nanomechanical resonator under investigation is a doubly clamped silicon nitride string resonator. It is 270 nm wide, 100 nm thick and 55 μm long and flanked by two adjacent gold electrodes for dielectric control. A schematic of the dielectric measurement setup is depicted in Fig. S2. A microwave signal (μw) is used to resonantly pump the microwave cavity, which is bonded to one of the electrodes. The transmitted and modulated microwave cavity signal (RF) is demodulated by IQ-mixing it with a reference signal (LO). The output signal is low-pass filtered (LP), amplified (AMP) and its frequency spectrum is recorded using a spectrum analyzer (SA). Only for the measurement shown in Fig. 1b of the main text as well as Fig. S3a and c a lock-in amplifier is employed. The dc voltage (dc) and the rf drive tone (rf) of frequency f_F are combined with a bias tee and applied to the other electrode. A microwave bypass enables the combination of dielectric actuation and detection. More details about the dielectric control scheme can be found in Refs. S10–S12.

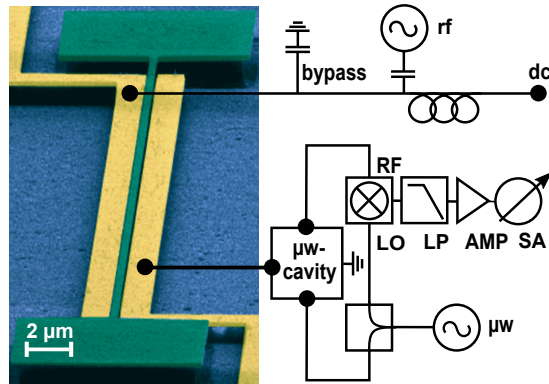


Figure S2. Simplified electronic set-up for dielectric actuation and displacement detection.

B. Calibration using the linear response function

In the measurement we cannot access the amplitude A and the force F directly. However we know the amplitude of the rf input voltage V_{in} that drives the capacitor containing the dielectric nanostring and we measure the output voltage signal V_{out} close to the eigenfrequency of the resonator ω_0 . We assume these quantities to be proportional to the driving strength F and to the amplitude A , respectively,

$$A = a V_{\text{out}} , \quad F = b V_{\text{in}} . \quad (\text{S32})$$

This allows us to calibrate the driving strength with the benefit of excluding a parameter for further analysis. For weak driving power, the resonator is in the linear regime and the vibration amplitude A is given by the well known Lorentzian response $A^2 = (F/2\omega_0)^2 / (\delta\omega^2 + \Gamma^2)$. Rewriting the Lorentzian response function with the use of Eq. (S32) leads to

$$V_{\text{out}}^2 = \frac{\Gamma^2}{\delta\omega^2 + \Gamma^2} \cdot c \cdot V_{\text{in}}^2 , \quad (\text{S33})$$

where the dimensionless parameter $c = (b/a)^2 / (4\omega_0^2\Gamma^2)$ is the calibration factor. At fixed rf input voltage V_{in} (or drive power), we fit V_{out} with the Lorentzian function Eq. (S33) (see Fig. S3a), yielding an eigenfrequency $f_0 = \omega_0/2\pi = 6.529$ MHz and a linewidth $2\Gamma/2\pi = 20$ Hz. The same linewidth is found by a ringdown measurement (see Fig. S3b). Driving the system on resonance ($\delta\omega = 0$) gives the maximum output signal $V_{\text{out},\text{max}}$, and it follows that $V_{\text{out},\text{max}}^2 = c V_{\text{in}}^2$. This procedure is repeated for different drive voltages V_{in} (expressed as drive power in the main text). The obtained ratios $V_{\text{out},\text{max}}^2/V_{\text{in}}^2$ are fit with the constant c . We obtained a calibration factor $c = 0.0062(3)$.

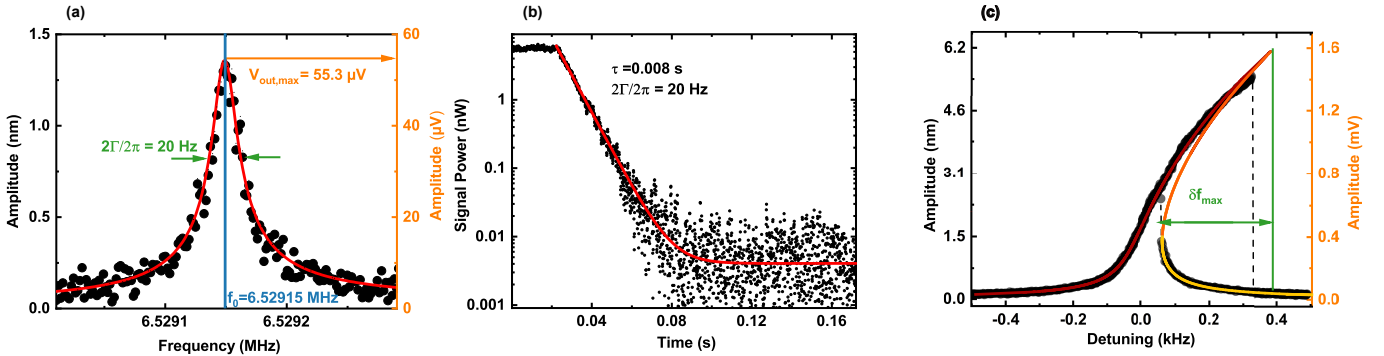


Figure S3. **a** Linear response measurement (black dots) as well as Lorentzian fit (red line) for the eigenfrequency and linewidth evaluation as well as for the driving strength calibration. **b**, Ringdown measurement (black dots) along with exponential fit (red line), confirming the linewidth measured in linear response. **c** Nonlinear response measurement (black dots) with fit of the Duffing model (red, yellow, and orange line represents stable high amplitude, stable low amplitude and unstable solution, respectively). Amplitude and frequency detuning of the backbone point highlighted in green are used for the amplitude calibration.

C. Duffing nonlinearity parameter

From Eq. (S5) one can express the detuning $\delta\omega$ in terms of the amplitude A of the forced vibrations on the high-amplitude branch. Using the scaling relations Eq. (S32), we can write

$$\frac{\delta\omega}{\Gamma} = \frac{3\tilde{\gamma}}{8\omega_0\Gamma} V_{\text{out}}^2 - \sqrt{c \left(\frac{V_{\text{in}}^2}{V_{\text{out}}^2} \right) - 1}, \quad (\text{S34})$$

where we have introduced an effective Duffing parameter $\tilde{\gamma} = \gamma \cdot a^2$ with dimension $[1/V^2 s^2]$. In the non-linear regime, we fit the nonlinear amplitude response function by plotting $\delta\omega$ as a function of the r.h.s. of Eq. (S34) with the high amplitude branch for V_{out} and using $\tilde{\gamma}$ as the single fitting parameter. For the power $P = -31$ dBm, which is used to obtain the results shown in Fig. 1b of the main text, and for $P = -30$ dBm shown in Fig. S3c we found the scaled Duffing parameter to be $\tilde{\gamma} = 2.35 \cdot 10^{15} \text{ V}^{-2} \text{ s}^{-2}$. With the measured calibration factor c , the scaled Duffing parameter $\tilde{\gamma}$, the eigenfrequency, and the decay rate of the mode, we have fully determined the parameters of the theoretical model, Eq.(1) of the main text, except for the scaling a .

D. Amplitude calibration via the Duffing backbone curve

In order to compare the theoretical and experimental results on the power spectra we need to scale the fluctuation intensity. We note that the fluctuation-dissipation relation on its own is not sufficient unless we know the actual displacement of the nanomechanical resonator at the antinode as well as its effective mass. From the linear relation $A = a V_{\text{out}}$, one has the relation $Q_{VV}(\omega) = Q(\omega)/a^2$ with $Q_{VV}(\omega)$ being the power spectrum of the output voltage, and $Q(\omega)$ being the power spectrum of the resonator displacement in the linear regime. In the absence of driving we expect $\int d\omega Q_{VV}(\omega) = k_B T / (2 m \omega_0^2 a^2)$. By measuring the power spectrum and calculating the total area of the Lorentzian, one can extract the coefficient a . However we can not resolve the thermal motion of the undriven nanostring in our system apparatus and therefore we use another strategy.

To convert the voltage signal (measured in volts) into displacement amplitude (measured in nm) we use the fact that, in the Duffing model, the maximum value of the amplitude of forced vibrations as a function of the frequency detuning is given by the so-called backbone equation

$$\frac{3\gamma}{8\omega_0} A_{\text{max}}^2 = \delta\omega_{\text{max}}, \quad (\text{S35})$$

in which $\delta\omega_{\text{max}}$ denotes the detuning at which the upper bifurcation point is reached. To relate the measured voltage $V_{\text{out},\text{max}}$ to the maximal displacement $A_{\text{max}} = V_{\text{out},\text{max}}/a$ we use the measured $\delta\omega_{\text{max}}$ and the value of γ that we calculate assuming that the nanoresonator is a string, the nonlinearity of which is solely determined by its geometric nonlinearity γ^* , using the expression

$$\gamma^* = \pi^4 \frac{E + \frac{3}{2}\sigma}{4l^4\rho} = 1.54 \cdot 10^{26} \text{ m}^{-2} \text{ s}^{-2}, \quad (\text{S36})$$

where E is the Young's modulus, σ the tensile stress and ρ the mass density. For our suspended silicon nitride nanostring (atop a fused silica substrate) the tensile stress is measured to be $\sigma = 1.46$ GPa, [S12] while Young's modulus yields $E = 169$ GPa [S13]. The density $\rho = 2800$ kg/m³ is reported in literature [S14].

In this way we relate the maximum of the Duffing backbone curve, measured in volts, to the amplitude measured in nm as shown in Fig. S3c. The found proportional factor $a = 3.9 \cdot 10^{-6}$ m/V is also used for the amplitude of the linear response measurement, plotted in Fig. S3a. It is important to compare the resulting Duffing nonlinearity parameter $\tilde{\gamma}^* = \gamma^* \cdot a^2$ determined from the calculated γ^* and the calibration factor a with the measured $\tilde{\gamma}$. We used $\gamma^* = 1.54 \cdot 10^{26}$ m⁻²s⁻², which gave us $a = 3.9 \cdot 10^{-6}$ m/V, and thus $\tilde{\gamma}^* = \gamma^* \cdot a^2 = 2.28 \cdot 10^{15}$ V⁻²s⁻². The fitted Duffing nonlinearity parameter is $\tilde{\gamma} = 2.35 \cdot 10^{15}$ V⁻²s⁻², which is in reasonably good agreement.

E. Additional data

As an additional measurement we apply a fixed detuning of 190 Hz to the actuation frequency (close to the measured critical switching point) and sweep the drive power from -45 dBm up to -4 dBm, comparable to the measurement under resonant drive in the main text (Fig. 2a). The resulting power spectra as a function of drive power are shown in Fig. S4a. In contrast to the data obtained for a resonant drive, we observe an additional, single lower frequency satellite. This satellite is observed for a weak drive (below -30 dBm). For a strong drive (above 15 dBm), two symmetrical satellites are observed, similarly to the data obtained for a resonant drive. In the regime in between, each power spectrum shows either the former or the latter satellites, such that both satellite branches are visible. By calculating the expected satellite splitting, we can assign the single satellite to the low amplitude state of the Duffing resonator (yellow circles) and the two symmetric satellites to the high amplitude state (red circles). In the intermediate drive range, the Duffing resonator is in the bistable regime and depending on the initial conditions the system chooses either the high or the low amplitude solution, consequently we see a switching behaviour between the two possible satellite branches. This is particularly apparent from Fig. S4b, which plots the amplitude response at the drive tone as a function of the drive power, as in Fig. 3b of the main text. For a weak drive (below -25 dBm), the resonator is always in the low amplitude state, whereas for a large drive (above 15 dBm), the system is only found in the high amplitude state. In the intermediate region, the amplitudes jump back and forth, leading to the behavior observed for the satellite branches. As before, the area of the satellites can be extracted by a Lorentzian fit and the calculated ratio of the areas is plotted in Fig. S4c. We can only report a ratio for the high amplitude solution, as only one of the two satellites of the low amplitude solution is resolved in the experiment. Again the calculated area ration is in a good agreement with the theory, where the red line corresponds to the

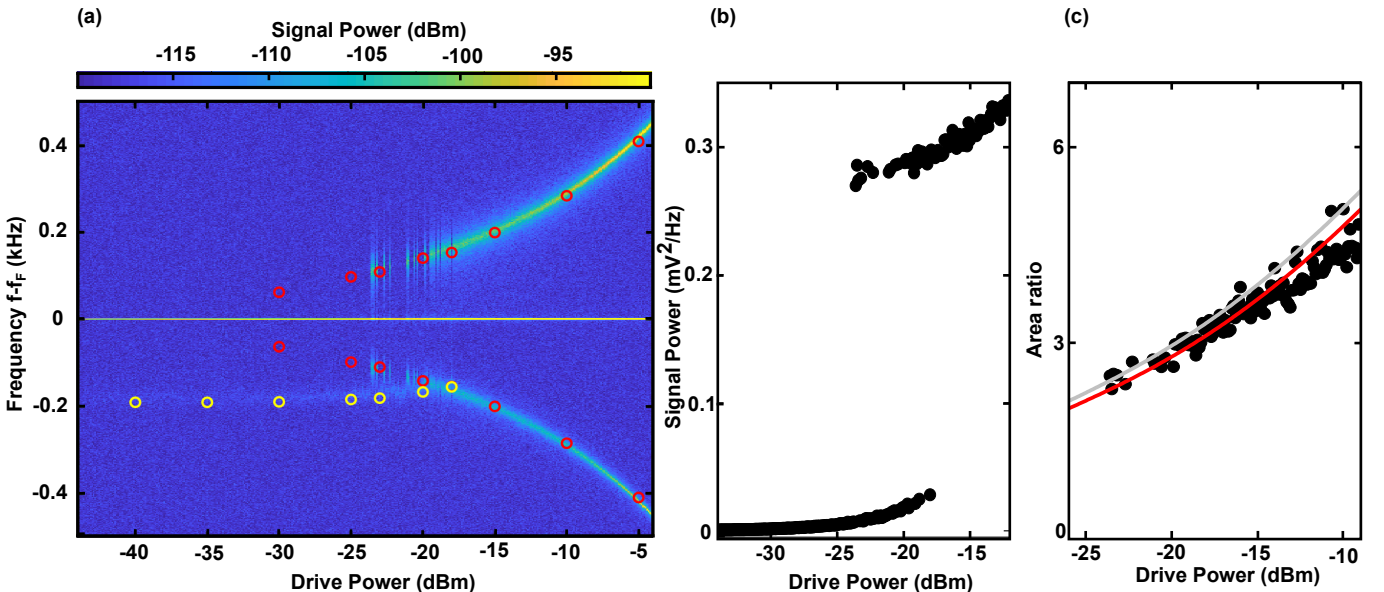


Figure S4. Power spectra as a function of the drive power for a fixed detuning of 190 Hz. (a) Color coded power spectra showing the satellite splitting and intensity as a function of the drive power. Red (yellow) open circles denote theoretically calculated satellite positions for the high (low) amplitude solution in the weak-damping approximation, that applies only where the satellite peaks are well-resolved. (b) Extracted amplitude of the response at the drive tone as a function of the drive power. (c) Ratio of the satellite areas when the resonator is in the high amplitude state. Gray (red) line shows the theoretical prediction in the weak damping approximation (more general linearized approximation taking into account the overlap of the satellite peaks).

theoretical calculation including the overlap of the two peaks and the gray line to the additional weak damping approximation.

[S1] M. I. Dykman and M. A. Krivoglaz, *Theory of fluctuational transitions between stable states of a non linear oscillator*, Soviet Physics JETP **50**, 30 (1979).

[S2] P. D. Drummond and D. F. Walls, *Quantum-theory of optical bistability. I: Non-linear polarizability model*, Journal of Physics A **13**, 725 (1980).

[S3] M. I. Dykman, D. G. Luchinsky, R. Mannella, P. V. E. McClintock, N. D. Stein, and N. G. Stocks, *Supernarrow spectral peaks and high-frequency stochastic resonance in systems with coexisting periodic attractors*, Physical Review E **49**, 1198 (1994).

[S4] C. Stambaugh and H. B. Chan, *Supernarrow Spectral Peaks near a Kinetic Phase Transition in a Driven Nonlinear Micromechanical Oscillator*, Physical Review Letters **97**, 110602 (2006).

[S5] D. F. Walls and G. J. Milburn, *Quantum Optics* (Springer, Berlin, 2008).

[S6] M. I. Dykman and M. A. Krivoglaz, *Theory of Nonlinear Oscillators Interacting with a Medium*, in *Sov. Phys. Reviews*, Vol. 5, edited by I. M. Khalatnikov (Harwood Academic, New York, 1984) pp. 265–441, web.pa.msu.edu/dykman/pub06/DKreview84.pdf.

[S7] M. I. Dykman, *Periodically modulated quantum nonlinear oscillators*, in *Fluctuating Nonlinear Oscillators: from Nanomechanics to Quantum Superconducting Circuits*, edited by M. I. Dykman (Oxford University Press, 2012) pp. 165–197.

[S8] V. I. Arnold, *Mathematical Methods of Classical Mechanics* (Springer, New York, 1989).

[S9] M. I. Dykman and M. A. Krivoglaz, *Classical theory of nonlinear oscillators interacting with a medium*, Physica Status Solidi B **48**, 497 (1971).

[S10] Q. P. Unterreithmeier, E. M. Weig, and J. P. Kotthaus, *Universal transduction scheme for nanomechanical systems based on dielectric forces*, Nature **458**, 1001 (2009).

[S11] J. Rieger, T. Faust, M. J. Seitner, J. P. Kotthaus, and E. M. Weig, *Frequency and Q factor control of nanomechanical resonators*, Applied Physics Letters **101**, 103110 (2012).

[S12] T. Faust, P. Krenn, S. Manus, J. P. Kotthaus, and E. M. Weig, *Microwave cavity-enhanced transduction for plug and play nanomechanics at room temperature*, Nature Communications **3**, 728 (2012).

[S13] Q. P. Unterreithmeier, T. Faust, and J. P. Kotthaus, *Damping of Nanomechanical Resonators*, Physics Review Letters **105**, 027205 (2010).

[S14] M. Gad-el Hak, *The MEMS Handbook* (CRC, Press, 2002).